4D Automotive Radar Sensing for Autonomous Vehicles: A Sparsity-Oriented Approach

Shunqiao Sun, *Senior Member, IEEE*, and Yimin D. Zhang, *Fellow, IEEE*

***Abstract*—We propose a high-resolution imaging radar system to enable high-fidelity four-dimensional (4D) sensing for autonomous driving, i.e., range, Doppler, azimuth, and elevation, through a joint sparsity design in frequency spectrum and array configurations. To accommodate a high number of automotive radars operating at the same frequency band while avoiding mutual interference, random sparse step-frequency waveform (RSSFW) is proposed to synthesize a large effective bandwidth to achieve high range resolution profiles. To mitigate high range sidelobes in RSSFW radars, optimal weights are designed to minimize the peak sidelobe level such that targets with a relatively small radar cross section are detectable without introducing high probability of false alarm. We extend the RSSFW concept to multi-input multi-output (MIMO) radar by applying phase codes along slow time to synthesize a two-dimensional (2D) sparse array with hundreds of virtual array elements to enable high-resolution direction finding in both azimuth and elevation. The 2D sparse array acts as a sub-Nyquist sampler of the corresponding uniform rectangular array (URA) with half-wavelength interelement spacing, and the corresponding URA response is recovered by completing a low-rank block Hankel matrix. Consequently, the high sidelobes in the azimuth and elevation spectra are greatly suppressed so that weak targets can be reliably detected. The proposed imaging radar provides point clouds with a resolution comparable to LiDAR but with a much lower cost. Numerical simulations are conducted to demonstrate the performance of the proposed 4D imaging radar system with joint sparsity in frequency spectrum and antenna arrays.**

***Index Terms*—Automotive radar, multi-input multi-output (MIMO) radar, autonomous driving, random sparse step-frequency waveform, interference mitigation, sparse array**

I. Introduction

RADAR sensors have found widespread applications in advanced driver assistance systems (ADAS), such as adaptive cruise control and automatic emergency braking. According to a National Highway Traffic Safety Administration (NHTSA) study, $37,461$ Americans died on the U.S. highways in 2016 as a result of automobile accidents [3], of which 94% were due to human error [4]. Radar has emerged as one of the key technologies in autonomous driving systems. Some of today's self-driving cars, such as Zoox, are equipped with more than 10 radars, providing a 360° surround sensing capability under all weather conditions [5]–[8]. Different from ground-based or airborne surveillance radars, automotive radars are strictly required to have a small size (multi-inch by multi-inch), short range (within multi-hundred meters), and low power (multi-Watt), so they can be integrated behind the vehicle bumper or windshield and operated in a highly dynamic propagation environment with rich multipath [9].

An automotive radar must provide high resolution in four dimensions (4D), i.e., range, Doppler, and azimuth and elevation angles, yet remain a low cost for feasible mass production. High-resolution imaging radar is being developed to provide point clouds of the surrounding environment [8], [10]–[12]. Via use of deep neural networks, such as PointNet [13] and PointNet++ [14], point clouds generated by high-resolution imaging radar can lead to adequate target identification. Automotive radar must also provide multiuser interference immunity to enable a high number of autonomous vehicles to operate at the same time.

As is well known, the range, Doppler, and angular resolution of an automotive radar are respectively determined by the waveform bandwidth, the coherent processing interval (CPI), and the antenna array aperture. To obtain high-resolution 4D radar imaging for autonomous driving, therefore, automotive radar needs to occupy a large bandwidth, a long CPI, and a large antenna aperture in both horizontal and vertical directions. The major challenges in achieving these goals are the lack of spectrum in the presence of a high number of automotive radars and the requirement of a high number of antennas needed to achieve the desired array aperture if a filled array is exploited. In this paper, we propose an automotive radar system design exploiting sparsity in both spectrum and antenna arrays without sacrificing the range and angular resolutions.

A. Prior Art on Automotive Radar Waveform

State-of-the-art automotive radar systems exploit frequency-modulated continuous-waveform (FMCW) signals at millimeter-wave frequencies [6]–[8] to enable high-resolution target range and velocity estimation, and can be implemented at a much lower cost than light detection and ranging (LiDAR). To achieve a high range resolution for autonomous driving, the transmit signals are designed to occupy a large bandwidth. For conventional automotive FMCW radars, the frequency linearly sweeps over the entire bandwidth, thereby making the signal susceptible to interference from other automotive radars. Alternatively, step-frequency waveform (SFW) radar transmits a sequence of pulses with linearly increased carrier frequencies to synthesize a wide bandwidth while keeping a low instantaneous bandwidth of each pulse so low sampling rate analog-to-digital converters (ADCs) can be used [15]. However, there is range-Doppler coupling in the conventional SFW radars.

S. Sun is with the Department of Electrical and Computer Engineering, The University of Alabama, Tuscaloosa, AL, USA (email: shunqiao.sun@ua.edu).

Y. D. Zhang is with the Department of Electrical and Computer Engineering, Temple University, Philadelphia, PA, USA (email: ydzhang@temple.edu).

Part of this work was presented in the 45th IEEE International Conference on Acoustics, Speech, and Signal Processing (ICASSP 2020) [1] and the 46th IEEE International Conference on Acoustics, Speech, and Signal Processing (ICASSP 2021) [2].

The sparse step-frequency waveform (SSFW) radar transmits several pulses within a large bandwidth, where some frequencies are unused during a CPI [16], [17]. Target parameters are estimated using compressive sensing (CS) methods [18]. An SSFW radar can avoid or reduce multiuser interference by skipping the spectrum bands that are occupied by other radars. However, use of SSFW radars will increase range sidelobes and, as a result, targets with a small radar cross section (RCS), such as pedestrian, may be obscured by high sidelobes of stronger targets.

B. High-Resolution Imaging Radar for Autonomous Driving

For autonomous driving, information in both azimuth and elevation is crucial. In particular, the height information of targets is required to enable drive-over and drive-under functions. Two typical scenarios are shown in Fig. 1. It is safe to drive over a metal beverage can on the road and to drive under a steel pedestrian bridge over the road. Automotive radars with limited capacity in measuring elevation angles will treat these objects as stationary blockage targets.

To meet such requirement, the array is required to have a large aperture in both azimuth and elevation. A cost-effective and scalable solution is to coherently cascade multiple automotive radar transceivers. The idea of virtual sum coarray has been extensively utilized in the multi-input multi-output (MIMO) radar literature [19] to achieve $M_t M_r$ virtual elements using only M_t transmit and M_r receive physical antennas. For example, cascaded radar chips rendering 12 transmit and 16 receive antennas are developed [20]–[22] to synthesize 192 virtual array elements using the MIMO radar technique, and several products are available with different array configurations, such as forward-looking full-range radar of ZF and ARS540 of Continental [23], [24].

One way to further reduce the cost without sacrificing the angular resolution is via the use of sparse arrays [25]–[27], synthesized with MIMO radar technology. Comparing to a large-size uniformly filled array, MIMO radar exploiting sparse arrays properly deploys a reduced number of transmit and receive antennas to achieve the same array aperture but the interelement spacing of the corresponding virtual array is larger than half wavelength. In other words, a sparse array is thinned from a uniformly filled array with the same aperture.

A closely related concept in sparse array exploitation is the direction-of-arrival (DOA) estimation using difference coarrays. When a sufficient number of snapshots are available, the difference coarray concept can be utilized either standalone or combined with the sum coarray concept to construct a coarray with significantly increased virtual sensors from a sparse physical array. Well-known sparse array configurations considered for difference coarray include the minimum redundancy array (MRA) [28], nested array [29], coprime array [30]–[32], and super nested array [33], [34]. The difference coarray concept provides a scheme to estimate more targets than the number of array elements. However, difference coarray requires a high number of snapshots to achieve accurate array covariance matrix estimation [35]. In a highly dynamic automotive scenario, however, the positions of both radar-mounted vehicle and objects may often change rapidly [8].

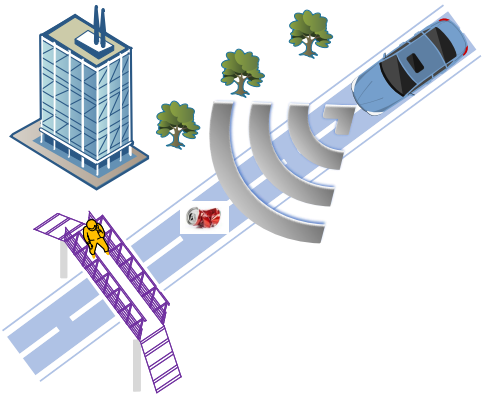

Figure 1: Automotive radars need to provide elevation resolution to enable drive-over and drive-under functions.

As a result, it is challenging to coherently process the targets echo measurements over a number of CPIs. In the worst case, only a single snapshot is available [36]. Therefore, it is often infeasible to apply the difference coarray concept that requires multiple snapshots in automotive radar. The array snapshot in this paper is defined as the array response of all virtual array elements corresponding to the same range-Doppler bin [8].

In both sum and difference coarrays, some sparse array configurations will render consecutive coarrays, i.e., there are no holes in the synthesized virtual array aperture. Examples of such order-wise sparse array configurations include the nested array used in both sum and difference coarray cases [29], [37]. On the other hand, when the lags in certain synthesized difference coarrays are not consecutive, such as the difference coarray of a coprime array, filling the holes to reconstruct a uniform linear array (ULA) with consecutive lags is shown to be effective to improve DOA estimation performance and apply certain DOA estimation methods, such as MUSIC with spatial smoothing [38], [39], that require a consecutive coarray configuration. Taking the advantage of the Toeplitz and Hankel properties of the covariance matrix of a ULA, several methods are developed to reconstruct sparse array covariance matrix using structured CS and structured matrix completion techniques [40]–[44].

In automotive radars, targets are typically first separated in range and Doppler domains. As a result, the number of targets that need to be resolved in the angular domain in the same range-Doppler bin is small [8]. Therefore, in this paper, instead of resolving more targets than the number of physical array elements using the difference coarray concept, we rather focus on obtaining a large virtual array aperture achieving high angular resolution in both azimuth and elevation directions with sum coarray-based sparse arrays exploiting only a *single snapshot*. The sum coarray construction in an active sensing scheme does not require the estimation of correlations and thus can be implemented using a single snapshot, as long as separable waveforms are used at the transmit end. This is fundamentally different to the difference coarray concept which requires a high number of snapshots to estimate the covariance matrix. Structured matrix completion is used to

fill the missing elements of covariance matrix to reduce the sidelobe levels and enable gridless DOA estimation [44]–[47].

C. Our Contributions

In this paper, we develop a 4D automotive MIMO radar sensing technique that provides point clouds at a much lower cost than LiDAR with higher robustness to weather conditions. Each transmit antenna transmits the same random sparse step-frequency waveform (RSSFW) to synthesize a large effective bandwidth for high-resolution range estimation, while keeping a low sampling rate. Sparse spectrum utilization also makes it insensitive to automotive radar interference. The waveform orthogonality is achieved through Doppler-division multiplexing (DDM). In the proposed MIMO radar using RSSFW waveforms, the targets are first separated in the range and Doppler domains, and a large virtual sparse array is synthesized and completed to provide high resolution in both azimuth and elevation.

The offerings of the proposed automotive radar system are summarized as:

1) It achieves high-resolution imaging capability with performance close to LiDAR systems but with a much lower cost. High resolution in range, Doppler, azimuth, and elevation is achieved via joint sparse spectrum and two-dimensional (2D) sparse array design. The sampling rate of ADC is kept low, and the hardware cost is reduced.

2) The RSSFW radar waveforms ensure low range sidelobe levels for reliable weak target detection. Optimal weights are designed to minimize the peak sidelobe level of the range spectrum so that targets with small RCS can be reliably detected without introducing high probability of false alarm.

3) The novel 2D sparse array interpolation technique reduces sidelobes and enables gridless angle estimation. We treat sparse arrays as a deterministic sub-Nyquist sampler of corresponding uniform arrays. The missing elements or holes in the sparse arrays are recovered by completing a low-rank Hankel matrix, and the recoverability is examined with respect to the Hankel matrix coherence and sparse array topology. Consequently, the sidelobes of irregular sparse arrays are suppressed so that the probability of false alarm in angle estimation or possible angle ambiguity can be mitigated. Furthermore, matrix completion enables gridless angle estimation with improved SNR.

4) It mitigates multiuser radar interference. Since only a small portion of the frequency spectrum is occupied, the proposed RSSFW radar enables flexible coordination of spectrum utilization among multiple automotive radars with low mutual interference among automotive radars.

The rest of the paper is organized as follows. We introduce the system model of RSSFW radar and present range sidelobe optimization and waveform orthogonality in Section II. High-resolution imaging radar with 2D sparse array and novel array interpolation are developed in Section III, and the recoverability of array completion is investigated in Section IV. Simulation results are presented in Section V. Finally, Section VI concludes the paper.

II. Sparse Step-Frequency-Based Automotive MIMO Radar

In this section, we address the problem of high-resolution target range estimation using RSSFW signals with a small number of carrier frequencies. We start with a simple single-transmit single-receiver model, and then extend it to a MIMO setting in Section II-C where the waveform orthogonality is addressed with slow-time phase codes.

Consider a sequence of N pulses whose carrier frequencies are a sparse subset chosen from P available frequencies, $\mathcal{M} = \{f_n | f_c + n\Delta f, n \in \{0, 1, \cdots, P-1\}\}$, that are equally distributed in $[f_c, f_c + B]$. The maximum unambiguous range is $R_u = c/(2\Delta f)$ whereas the range resolution is given by $\Delta R = c/(2P\Delta f) = R_u/P$. The total time duration of a burst cycle, T, consists of both transmit and receive modes. One CPI consists of M burst cycles. The unit-energy waveform of the n-th transmit pulse during the m-th burst cycle is expressed as

$$s(m,n,t) = \frac{1}{\sqrt{T_p}} \text{rect}\left(\frac{t - nT_p - mT}{T_p}\right) e^{j2\pi f_n \left(t - nT_p - mT\right)}, \tag{1}$$

where t is the fast time, T_p is the duration of each pulse, and

$$\text{rect}\left(\frac{t-\tau}{T_p}\right) = \begin{cases} 1, & \tau - T_P \le t \le +\tau, \\ 0, & \text{otherwise.} \end{cases} \tag{2}$$

Consider K point targets in the far field, and the k-th target has range r_k, radial velocity v_k, and complex reflection coefficient β_k. The received signal of the n-th pulse at the m-th slow time corresponding to the k-th target is

$$\tilde{y}_k(m,n,t) = \beta_k s\left(m, n, t - 2r_k(t)/c\right), \tag{3}$$

where $r_k(t) = r_k(0) + v_k t$ and c is the speed of light. After demodulation, the n-th echo is obtained as

$$y_k(m,n) = \beta_k e^{-j\frac{4\pi}{c} f_n \left[r_k(0) + \left(mT + nT_p\right)v_k\right]}. \tag{4}$$

The sampled received signal for the n-th pulse is the superposition of the echoes from all K targets, i.e.,

$$\begin{aligned} y(m,n) &= \sum_{k=1}^{K} y_k(m,n) \\ &= \sum_{k=1}^{K} \beta_k e^{-j\frac{4\pi}{c} f_n \left[r_k(0) + \left(mT + nT_p\right)v_k\right]} \\ &= \sum_{k=1}^{K} \gamma_k e^{-j\frac{4\pi}{c}\left(f_c m T v_k + h_n \Delta f r_k(0)\right)} \\ &\quad \times e^{-j\frac{4\pi}{c}\left(h_n \Delta f n T_p v_k + h_n \Delta f m T v_k + f_c n T_p v_k\right)}, \end{aligned} \tag{5}$$

where $\gamma_k = \beta_k e^{-j\frac{4\pi}{c} f_c r_k(0)}$.

We make the following assumptions:

A1) The unambiguous scope of high range resolution profiles (HRRP) defined as $c/(2\Delta f)$ should be larger than the scope of a range bin $cT_p/2$. This yields that $\Delta f < 1/T_p$.

A2) The range migration is negligible during one CPI, i.e., $v_k MT < cT_p/2$.

A3) Define $\xi_{m,n} = 2\big(2n\Delta f T_p + m\Delta f T + 2f_c T_p\big) v_k/c$. Considering the vehicle speeds in a typical autonomous driving scenario, it is reasonable to assume $\xi_{m,n} \ll 1/P$ for $m = 0, \cdots, M-1$ and $n = 0, \cdots, P-1$.

A4) The Doppler shift is considered constant in one burst cycle T because of the short duration of the burst pulses.

A. Range and Doppler Estimation in RSSFW Radar

Traditional step-frequency radar systems require $N = P$ pulses to achieve a range resolution of R_u/P. For the proposed sparse step-frequency approach, we use $N < P$ pulses and still achieve the same range resolution of R_u/P.

Stack the samples of one CPI with M burst cycles as matrix $\mathbf{Y} = [\mathbf{y}_1, \cdots, \mathbf{y}_M] \in \mathbb{C}^{P\times M}$. Each column contains fast-time samples $\mathbf{y}_m = [y(m,1), \cdots, y(m,P)]^T$ for $m = 1, \cdots, M$, where $(\cdot)^T$ stands for transpose. For the unused frequency carrier subset $\bar{\mathcal{M}}$ with $\left|\bar{\mathcal{M}}\right| = P-N$, the samples $y(m,i), i \in \bar{\mathcal{M}}$, are zero. Applying IDFT to the m-th column and noting that $h_n = n$ for $n = 0, 1, ..., P-1$, we obtain

$$\begin{aligned} F_m(l) =& \frac{1}{P}\sum_{n=0}^{P-1} y(m,n)\, e^{j2\pi\frac{l}{P}n} \\ =& \frac{1}{P}\sum_{k=1}^{K} \gamma_k e^{-j\frac{4\pi}{c}f_c m T v_k} e^{j\pi(P-1)\left(\frac{l}{P}-\frac{2r_k(0)}{c}\Delta f-\xi_{m,n}\right)} \\ & \times \frac{\sin\left(\pi\left(\frac{l}{P}-\frac{2r_k(0)}{c}\Delta f-\xi_{m,n}\right)P\right)}{\sin\left(\pi\left(\frac{l}{P}-\frac{2r_k(0)}{c}\Delta f-\xi_{m,n}\right)\right)}. \end{aligned} \tag{6}$$

Under assumption (**A3**), i.e., $\xi_{m,n} \ll 1/P$, $F_m(l)$ achieves its maximum magnitude when $l_k = 2r_k(0)P\Delta f/c$, and the target range is calculated as $r_k(0) = cl_k/(2P\Delta f) = \Delta R l_k$.

For each range bin l, the velocity estimation is obtained by applying discrete Fourier transform (DFT) to the obtained range spectra $F_m(l)$ for $m = 0, 1, \cdots, M-1$, given as

$$D_l(k) = \sum_{m=0}^{M-1} F_m(l)\, e^{-j2\pi\frac{k}{M}m}. \tag{7}$$

P-point IDFT for range estimation and M-point DFT for Doppler estimation provide $10\log_{10}(PM)$ dB SNR enhancement [8]. This SNR enhancement is considered as a processing gain which significantly benefits the angle estimation.

B. Range Sidelobe Minimization via Optimal Weighting

As we discussed earlier, since the carrier frequencies are uniformly divided and randomly chosen, the range spectrum would have high sidelobes. As a result, targets with a small RCS may be obscured by the range sidelobes of stronger targets.

This problem can be effectively solved using CS methods, possibly combined with the matrix completion methods discussed in Section III. CS-based approaches, however, requires a high computational cost and is subject to off-grid issue [48]. In this subsection, we introduce a simpler alternative solution using optimized weights.

Denote w_n as the complex weight for each sparsely allocated carrier frequency $f_n \in [f_c, f_c + B]$, and let $\mathbf{w} = [w_1, \cdots, w_P]^T$, where $w_n = 0$ if $f_n \notin [f_c, f_c + B]$. The IDFT of the weighted fast-time samples can be written as

$$F_m(l) = \frac{1}{P}\sum_{n=0}^{P-1} w_n y(m,n)\, e^{j2\pi\frac{l}{P}n}. \tag{8}$$

In the above equation, the received range data $\mathbf{y}_m$ in the m-th burst cycle is multiplied with sparse weights $\mathbf{w}$ before Fourier transform is performed to get range spectrum. According to the signal processing theory, in the frequency domain, the obtained range spectrum will be the convolution of frequency response of sparse weights $\mathbf{w}$ and frequency response of the original range data $\mathbf{y}_m$. Therefore, the spectrum of the sparse weights $\mathbf{w}$ is desired to have low sidelobe levels over the entire sidelobe region so that the possible high range sidelobes in the resulting convolution would be minimized.

To obtain the optimal weight vector, we discretize the entire unambiguous range R_u into a fine grid of Q points, r_q, $q = 1, \cdots, Q$, separated by ΔR, and set $r_f = R_u/2$ as the range corresponding to mainlobe. The sidelobe area is then described by set $\mathcal{Q} = \{r_1, \cdots, r_f - \Delta R, r_f + \Delta R, \cdots, R_u\}$. Define a range steering vector with respect to range r_q as $\mathbf{b}(r_q) = [b_1(r_q), \cdots, b_P(r_q)]^T$, where

$$b_n(r_q) = \begin{cases} e^{-j2\pi\frac{2r_q}{c}f_n}, & \text{if } f_n \in \mathcal{M}, \\ 0, & \text{if } f_n \notin \mathcal{M}. \end{cases} \tag{9}$$

The power spectrum of the ranges corresponding to sidelobe in $\mathcal{Q}$ is constrained to be below a threshold η determined by peak sidelobe level (PSL), i.e., $\eta = 10^{V_{\max}/10}$, where $V_{\max}$ is the maximum allowed PSL in dB. The weight optimization can be viewed as a range sidelobe minimization problem and is formulated as

$$\begin{aligned} \min_{\mathbf{w},\alpha}\ & \alpha \\ \text{s.t.}\ & \left|\mathbf{w}^H\mathbf{b}(r_q)\right| \le \eta + \alpha, \quad r_q \in \mathcal{Q}, \\ & \mathbf{w}^H\mathbf{b}(r_f) = 1, \end{aligned} \tag{10}$$

where $(\cdot)^H$ denotes conjugate transpose. The above optimization problem is convex and can be solved efficiently via CVX toolbox [49].

C. Waveform Orthogonality for RSSFW

In one CPI, a total number of M burst pulse cycles are transmitted. All transmit antennas simultaneously transmit the RSSFW waveform at the same sparse carrier frequencies. We adopt phase coding in slow time to achieve waveform orthogonality via DDM. Each pulse has the same phase code in one burst cycle, and the phase code varies with different burst pulse cycles. The phase code for the m_1-th transmit antenna is given as $x_{m_1}(m) = e^{j2\pi\alpha_{m_1}(m)}$ for $m_1 = 1, \cdots, M_t$ and $m = 1, \cdots, M$ [50]. To separate the m_1-th transmit signal at a receiver, after range IDFT, a slow-time Doppler demodulation is applied to all range bins corresponding to the same pulse. The demodulated outputs of the M burst pulse cycles are assembled into a vector, and its DFT yields the Doppler outputs. The slow-time phase codes are designed such that the waveform residual from other transmit antennas is equally distributed over the whole Doppler spectrum.

The benefit of using slow-time phase coding is that the interference from other transmitters does not affect different range bins. The range resolution is determined only by the effective bandwidth of the synthesized RSSFW waveform.

III. High-Resolution Imaging Radar Systems with Sparse Array Design

Depending on the performance and cost requirement, automotive radar can use one or multiple transceivers to synthesize a sparse linear array (SLA) for direction finding. The utilization of sparse arrays not only reduces the hardware cost but also reduce mutual coupling effects among antennas since the interelement spacing in both transmit and receive arrays is kept sufficient large. The array response at a particular time instance consisting of data obtained at all the $M_t M_r$ virtual receivers and corresponding to the same range-Doppler bin is defined as an *array snapshot*. To mitigate the high sidelobes introduced by the sparse arrays, we utilize the matrix completion technology to interpolate/extrapolate the holes in the sparse arrays. Furthermore, matrix completion improves the SNR of array response as there is no loss/holes in the fully recovered arrays.

During one CPI of a typical automotive radar scenario, a dense point cloud with a high volume of targets could be detected in the range-Doppler spectrum [11]. The success of applying matrix completion in irregular one-dimensional (1D) or 2D sparse arrays relies on the following two facts:

F1) The number of targets in the same range-Doppler bin that need angle estimation is small since the targets are first separated in range-Doppler domain by exploiting the RSSFW. In other words, the targets are sparsely present in the angular domain and, as a result, the Hankel matrix constructed using the array response is low rank.

F2) The SNR in the array snapshot is much higher than that in the echo signal, since energy has been accumulated in both range and Doppler domains via the IDFT and DFT operations. The high SNR in the array snapshot help reduce the matrix completion error and improve the accuracy of angle estimation.

We will illustrate the array interpolation concept through matrix completion in one-dimensional sparse arrays and then extend it to two-dimensional sparse arrays.

A. One-Dimensional Sparse Array Design

Fig. 2 shows an example of the physical array configuration of an automotive radar which is a cascaded of 2 MIMO transceivers, where all transmit and receive antennas are clock synchronized. Let λ denote the wavelength of the carrier frequency. In this example, $M_t = 6$ transmit and $M_r = 8$ receive antennas are deployed on discretized grid points along the azimuth direction with an interval of length equal to 50λ. The interval is discretized uniformly with half-wavelength spacing. The transmit antennas transmit RSSFW waveform in a way that, at each receive antenna, the contribution of each transmit antenna can be separated via DDM. Therefore, with MIMO radar technology, a virtual SLA with 48 array elements and aperture of 75λ is synthesized, as shown in

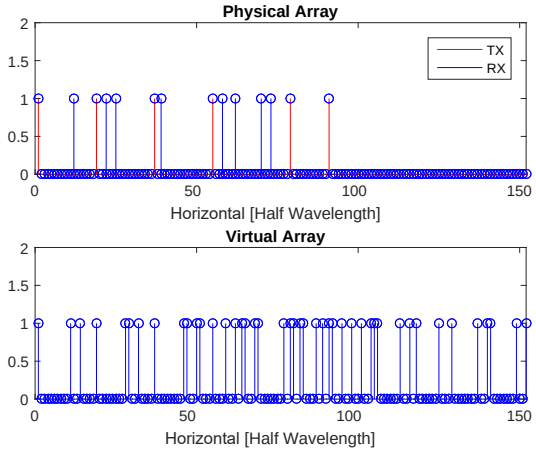

Figure 2: Example of an automotive radar cascaded with two transceivers. The virtual array has 48 elements.

Fig. 2. Compared to a ULA with half-wavelength interelement spacing and the same aperture, a high number of elements at certain locations are "missing" at the rednered virtual SLA (denoted by zeros in the virtual array of Fig. 2). However, the SLA approach uses only $M_t + M_r = 14$ physical antennas with significantly reduced mutual coupling effects [8].

Suppose an array snapshot contains K targets with DOAs $\theta_k,\ k = 1, \cdots, K$. Without noise, the SLA response can be expressed as

$$\mathbf{y}_S = \mathbf{A}_S \mathbf{s}, \tag{11}$$

where $\mathbf{A}_S = [\mathbf{a}_S(\theta_1), \cdots, \mathbf{a}_S(\theta_K)]$ is the manifold matrix with $\mathbf{a}_S(\theta_k) = \left[1, e^{j\frac{2\pi}{\lambda} d_1 \sin(\theta_k)}, \cdots, e^{j\frac{2\pi}{\lambda} d_{M_t M_r - 1} \sin(\theta_k)}\right]^T$, and d_i is the distance between the i-th element of SLA and the reference element. In addition, $\mathbf{s} = [\beta_1, \cdots, \beta_K]^T$, where β_k denotes the amplitude associated with the k-th target.

Consider a virtual ULA that spans the entire array aperture and is filled with antennas spaced by interelement spacing $d = \lambda/2$. The total number of antennas in this virtual ULA is M_o and the noiseless array response is expressed as

$$\mathbf{y}_o = \mathbf{A}_o \mathbf{s}, \tag{12}$$

where $\mathbf{A}_o = [\mathbf{a}_o(\theta_1), \cdots, \mathbf{a}_o(\theta_K)]$ is the array manifold matrix with $\mathbf{a}_o(\theta_k) = \left[1, e^{j\pi \sin(\theta_k)}, \cdots, e^{j\pi(M_o - 1)\sin(\theta_k)}\right]^T$.

Let $N_2 = \lfloor M_0/2 \rfloor$ and $N_1 = M_0 - N_2 \geq N_2$. We can formulate $\mathbf{y} \in \mathbb{C}^{M_o \times 1}$ into N_2 overlapped subarrays of length N_1. Based on those subarrays, we formulate a Hankel matrix $\mathbf{Y} \in \mathbb{C}^{N_1 \times N_2}$ with its (i,j)-th element given as $\mathbf{Y}_{ij} = \mathbf{y}_{i+j-1}$ for $i = 1, \cdots, N_1$ and $j = 1, \cdots, N_2$. The Hankel matrix $\mathbf{Y}$ has a Vandermonde factorization [51], expressed as

$$\mathbf{Y} = \mathbf{B}\mathbf{\Sigma}\mathbf{B}^T, \tag{13}$$

where $\mathbf{B} = [\mathbf{b}(\theta_1), \cdots, \mathbf{b}(\theta_K)]$ is the subarray manifold matrix with $\mathbf{b}(\theta_k) = \left[1, e^{j\frac{2\pi}{\lambda} d \sin(\theta_k)}, \cdots, e^{j\frac{2\pi}{\lambda}(N-1) d \sin(\theta_k)}\right]^T$, and $\mathbf{\Sigma} = \mathrm{diag}(\beta_1, \cdots, \beta_K)$ is a diagonal matrix. Thus, the rank of Hankel matrix $\mathbf{Y}$ is K if $N_2 \geq K$.

We can similarly construct a Hankel matrix $\mathbf{X}$ from the SLA configuration. Unlike matrix $\mathbf{Y}$ constructed from a full ULA,

however, matrix $\mathbf{X}$ has many missing entries and thus can be viewed as a subsampled version of $\mathbf{Y}$. Under certain conditions, the missing elements can be fully recovered by solving a relaxed nuclear norm optimization problem conditioned on the observed entries [52]

$$\min \ \|\mathbf{X}\|_* \quad \text{s.t.} \ \ \mathcal{P}_\Omega(\mathbf{X}) = \mathcal{P}_\Omega(\mathbf{Y}) \tag{14}$$

where $||\cdot||_*$ denotes the nuclear norm of a matrix, and $\mathcal{P}_\Omega(\mathbf{Y})$ is the sampling operator with Ω being the set of indices of observed entries that is determined by the SLA. In practice, the samples are corrupted by noise, i.e., $[\mathbf{X}]_{ij} = [\mathbf{Y}]_{ij} + [\mathbf{E}]_{ij}, (i,j) \in \Omega$, where $[\mathbf{E}]_{ij}$ denotes the noise. In this case, the matrix completion problem is formulated as

$$\min \ \|\mathbf{X}\|_* \quad \text{s.t.} \quad \|\mathcal{P}_\Omega(\mathbf{X} - \mathbf{Y})\|_{\mathrm{F}} \leq \delta \tag{15}$$

where $\|\cdot\|_{\mathrm{F}}$ denotes the Frobenius norm of a matrix and δ is a constant determined by the noise power.

Once the matrix $\mathbf{Y}$ is recovered, the full array response is obtained by averaging its anti-diagonal entries. DOAs can be estimated via standard array processing methods based on the array response corresponding to the completed matrix $\mathbf{Y}$.

B. Two-Dimensional Sparse Array Design

As we discussed earlier, to enable driver-over and driver-under functions, automotive radar must measure target's elevation angles accurately. As a result, automotive radar needs to provide point clouds with high angular resolution in both azimuth and elevation directions. Fig. 3 shows a MIMO radar with 12 transmit antennas and 16 receive antennas that are obtained by cascading 4 automotive radar transceivers, and the transmit and receive antennas are randomly deployed in an area of $[0, 100](\lambda/2) \times [0, 120](\lambda/2)$ to synthesize a MIMO 2D virtual sparse array of 196 elements. The 2D physical array corresponds to a form factor of about 20×24 cm when the carrier frequency is $f_c = 77$ GHz. It should be noted that a tradeoff between the angular resolution and the radar form factor should be considered in practice so that the radar can be incorporated behind vehicle bumper. The dimension of the rendered 2D virtual sparse array is $D_y \times D_x = 183(\lambda/2) \times 194(\lambda/2)$, which can be viewed as a spatial sub-Nyquist sampling of a uniform rectangular arrays (URA) of the same dimension with half-wavelength spacing in both horizontal and vertical directions. The azimuth and elevation angular resolutions are respectively expressed as [15]

$$\Delta\theta = 2\arcsin\left(\frac{1.4\lambda}{\pi D_x}\right) \approx 0.53^\circ, \tag{16}$$

$$\Delta\phi = 2\arcsin\left(\frac{1.4\lambda}{\pi D_y}\right) \approx 0.56^\circ. \tag{17}$$

The angular resolution of imaging radar in this example is comparable to the Velodyne LiDAR HDL-32E whose horizontal resolution is between 0.1° and 0.4° depending on the rotation rate, and the vertical resolution is 1.33° [53].

Consider a general case of an $M_1 \times M_2$ URA with half-wavelength spacing, shown in Fig. 4, where the URA is on the x-y plane. Assume the k-th point target with azimuth angle θ_k and elevation angle ϕ_k. Let χ_k denote the angle between the

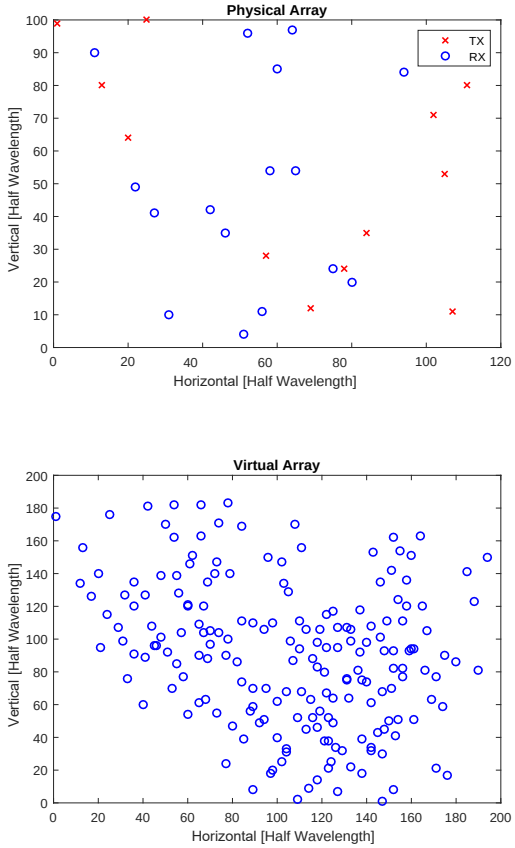

Figure 3: A MIMO radar with 12 transmit antennas and 16 receive antennas by cascading 4 automotive radar transceivers. The transmit and receive antennas are randomly deployed in an area of $[0, 100](\lambda/2) \times [0, 120](\lambda/2)$ to synthesize a MIMO 2D virtual array of 196 elements.

k-th target and the x axis, and φ_k denote the angle between the k-th target and the y axis. Then, it holds that $\cos(\chi_k) = \sin(\phi_k)\cos(\theta_k)$, $\cos(\varphi_k) = \sin(\phi_k)\sin(\theta_k)$. Therefore,

$$\theta_k = \arctan\left(\frac{\cos(\varphi_k)}{\cos(\chi_k)}\right), \tag{18}$$

$$\phi_k = \arcsin\left(\sqrt{\cos^2(\chi_k) + \cos^2(\varphi_k)}\right). \tag{19}$$

Once the angles χ_k and φ_k are known, the azimuth angle θ_k and elevation angle ϕ_k can be uniquely determined. To simplify the signal modeling, we use angles χ_k and φ_k for signal modeling in URA.

The (m_1, m_2)-th element of the URA array on the x-y plane response with respect to K targets with angle to the x-axis χ_k and angle to the y-axis φ_k, $k = 1, ..., K$, can be written as

$$x_{m_1,m_2} = \sum_{k=1}^{K} \beta_k e^{j\pi((m_1-1)\sin(\chi_k)+(m_2-1)\sin(\varphi_k))} \tag{20}$$

for $1 \leq m_1 \leq M_1$ and $1 \leq m_2 \leq M_2$. Let $\mathbf{M} = \left[x_{m_1,m_2}\right]_{0\leq m_1\leq M_1, 0\leq m_2\leq M_2}$ be the data matrix with entries

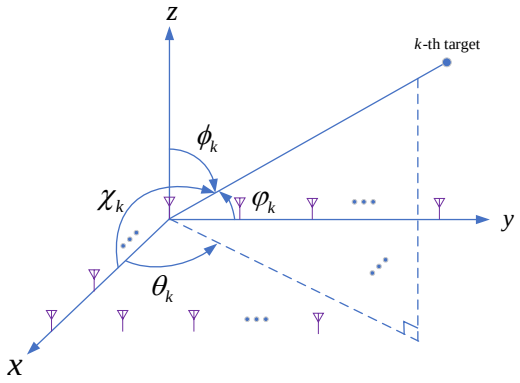

Figure 4: Geometry of URA.

as the URA array response defined in (20). We can construct an $N_1 \times (M_1 - N_1 + 1)$ block Hankel matrix as

$$\mathbf{Y}_E = \begin{bmatrix} \mathbf{Y}_0 & \mathbf{Y}_1 & \cdots & \mathbf{Y}_{M_1-N_1} \\ \mathbf{Y}_1 & \mathbf{Y}_2 & \cdots & \mathbf{Y}_{M_1-N_1+1} \\ \vdots & \vdots & \ddots & \vdots \\ \mathbf{Y}_{N_1-1} & \mathbf{Y}_{N_1} & \cdots & \mathbf{Y}_{M_1-1} \end{bmatrix}, \tag{21}$$

where

$$\mathbf{Y}_m = \begin{bmatrix} x_{m,0} & x_{m,1} & \cdots & x_{m,M_2-L} \\ x_{m,1} & x_{m,2} & \cdots & x_{m,M_2-L+1} \\ \vdots & \vdots & \ddots & \vdots \\ x_{m,L-1} & x_{m,L} & \cdots & x_{m,M_2-1} \end{bmatrix}, \tag{22}$$

is an $L \times (M_2 - L + 1)$ Hankel matrix. It can be verified that the rank of matrix $\mathbf{Y}_E$ is K if $N_1 \geq K$ and $L \geq K$ [54].

By choosing the locations of the transmit and receive antennas, we aim to synthesize a sparse 2D array, which can be viewed as spatial subsampling of the URA. The array response of the URA can be obtained via completing the block Hankel matrix $\mathbf{Y}_E$ based on the array response of sparse arrays. The block Hankel matrix completion problem is formulated as

$$\min \|\mathbf{X}_E\|_* \quad \text{s.t.} \quad \mathcal{P}_\Omega(\mathbf{X}) = \mathcal{P}_\Omega(\mathbf{M}) \tag{23}$$

where Ω denotes the observation set consisting of the location of 2D sparse virtual array elements, and $\mathbf{X}_E$ is the block Hankel matrix constructed from matrix $\mathbf{X}$ following equations (21) and (22). In the noisy observation scenario, $\mathbf{M}$ is replaced by $\mathbf{M}^o = \left[x^o_{m_1,m_2}\right]_{0\leq m_1\leq M_1, 0\leq m_2\leq M_2}$ with $x^o_{m_1,m_2} = x_{m_1,m_2} + n_{m_1,m_2}$, where $x^o_{m_1,m_2}$ denotes the observed signal and $\mathbf{E} = \left[n_{m_1,m_2}\right]_{0\leq m_1\leq M_1, 0\leq m_2\leq M_2}$ is the noise term. We assume the noise is bounded, i.e., $\|\mathcal{P}_\Omega(\mathbf{E})\|_{\mathrm{F}} \leq \delta$. The noisy block Hankel matrix completion problem is formulated as

$$\min \|\mathbf{X}_E\|_* \quad \text{s.t.} \quad \|\mathcal{P}_\Omega(\mathbf{X} - \mathbf{M}^o)\|_{\mathrm{F}} \leq \delta. \tag{24}$$

The above optimization problem can be solved in CVX toolbox [49]. In this paper, we adopt the singular value thresholding (SVT) algorithm [55] to solve the matrix completion problems, whose computation cost of updating the low-rank matrix in each iteration is of order m with m being the cardinality of the observation set Ω, i.e., $m = |\Omega|$.

C. Angle Finding With Completed Full Arrays

Once the Hankel matrix or block Hankel matrix is completed, direction finding can be performed using the matrix pencil method [54], [56]. Alternatively, the array response can be obtained from the recovered matrices and direction finding can be carried out using digital beamforming (DBF) [57] by performing fast Fourier transform (FFT) on snapshots taken across the array elements. DBF can be implemented efficiently in an embedded digital signal processor with a single snapshot. However, DBF is not a high-resolution direction finding method. Higher-resolution direction finding can be achieved with subspace based methods, such as MUSIC [58] and ESPRIT [59], and sparse sensing based methods [31], [60]–[65]. The performance of subspace based direction finding methods relies on accurate estimation of the array covariance matrix with multiple snapshots, which is a challenging task in highly non-stationary automotive radar scenarios. While sparse sensing based methods have high computational cost, they yield angle estimates based on a single snapshot, which is important for snapshot-limited automotive radar.

IV. Recoverability of Array Completion

The identifiability of full arrays via matrix completion from a sparsely populated array is related to several factors, e.g., the coherence properties of the constructed Hankel matrix and the sparse array topology, i.e., the locations of spatial sub-Nyquist sampling entries. In this section, we separately examine these two factors to determine whether holes in a sparse array can be completed via matrix completion.

A. Matrix Coherence and Recovery Performance

Let $\mathbf{U}$ and $\mathbf{V}$ be left and right subspaces of the singular value decomposition of Hankel matrix $\mathbf{Y} \in \mathbb{C}^{N\times N}$, which has rank K. The coherence of $\mathbf{U}$ (similarly for $\mathbf{V}$) equals [52]

$$\mu(U) = \frac{N}{K} \max_{1\leq i\leq N} \|\mathbf{U}(i,:)\|^2 \in \left[1, \frac{N}{K}\right]. \tag{25}$$

Matrix $\mathbf{Y}$ has coherence with parameters μ_0 and μ_1 if

B1) $\max(\mu(U), \mu(V)) \leq \mu_0$ holds for some positive μ_0.

B2) The maximum element of matrix $\sum_{1\leq i\leq K} \mathbf{u}_i \mathbf{v}_i^H$ is upper bounded by $\mu_1\sqrt{K}/N$ in absolute value for some positive μ_1.

The following theorem relates the coherence of Hankel matrix $\mathbf{Y}$ to the the number of targets, the relative location of targets, and N.

Theorem 1. *(Coherence of Hankel Matrix $\mathbf{Y}$): Consider the Hankel matrix $\mathbf{Y}$ constructed from a uniform linear array as presented in Eq. (13) and assume that the set of target angles $\{\theta_k\}_{k\in\mathbb{N}_K^+}$ consists of almost surely distinct members, with minimal spatial frequency separation $x = \min_{(i,j)\in\mathbb{N}_K^+\times\mathbb{N}_K^+, i\neq j} \frac{d}{\lambda}(\sin\theta_i - \sin\theta_j)$ satisfying $|x| \geq \xi \neq 0$. If $K \leq \sqrt{\frac{N}{\beta_N(\xi)}}$ where $\beta_N(\xi) = \frac{1}{N}\frac{\sin^2(\pi N\xi)}{\sin^2(\pi\xi)}$ is the Fejér kernel, the matrix $\mathbf{Y}$ satisfies the conditions (**B1**) and (**B2**) with coherence parameters*

$$\mu_0 \triangleq \frac{\sqrt{N}}{\sqrt{N} - (K-1)\sqrt{\beta_N(\xi)}} \tag{26}$$

and $\mu_1 \triangleq \mu_0\sqrt{K}$ *with probability* 1.

Proof. See Appendix A. □

The Fejér kernel $\beta_N(x)$ is a periodic function of x. For $d = \lambda/2$, the spatial frequency separation satisfies $|x| \in (0, 1/2]$. If $0 < \xi < 1/N$, it holds that $\beta_N(\xi) = \mathcal{O}\left(1/\sqrt{N}\right)$. Increasing the number of subarray elements N will decrease μ_0. It holds that $\lim_{N\to\infty} \mu_0 = 1$, which is its smallest possible value.

Let $m = |\Omega|$ be the cardinality of the observation set Ω. It was shown in [52] that, when entries of matrix $\mathbf{Y}$ are observed uniformly at random, there are constants C and c such that if

$$m \geq C \max\left(\mu_1^2, \mu_0^{1/2}\mu_1, \mu_0 N^{1/4}\right) \zeta K N \log N \tag{27}$$

holds for some $\zeta > 2$, the minimizer to problem (14) is unique and equals to $\mathbf{Y}$ with probability of $1 - cN^{-\zeta}$. Therefore, if matrix $\mathbf{Y}$ has a low coherence parameter, it can be completed using a less number of observed entries. In the noisy observation case, assuming the noise is zero-mean with variance σ^2, the noise term is defined as $\delta^2 = \left(m + \sqrt{8m}\right)\sigma^2$. Let $\hat{\mathbf{Y}}$ be the solution to the nuclear norm minimization problem of (15). The error norm is bounded by $\|\hat{\mathbf{Y}} - \mathbf{Y}\|_{\mathrm{F}} \leq 4\delta\sqrt{(2N^2 + m)N/m} + 2\delta$ with a high probability [66].

It was shown in [67] that block Hankel matrix $\mathbf{Y}_E$ follows the coherence properties with parameter μ_1 if any two targets are sufficiently separated. In the noisy observation case, if the number of random measurements satisfies

$$m > c_1\mu_1 c_s K \log^4(M_1 M_2), \tag{28}$$

where $c_s = \max\left\{\frac{M_1M_2}{N_1L}, \frac{M_1M_2}{(M_1-N_1+1)(M_2-L+1)}\right\}$ and c_1 is a constant, the solution of problem (24), $\hat{\mathbf{X}}_E$, satisfies $\|\hat{\mathbf{X}}_E - \mathbf{X}_E\|_{\mathrm{F}} \leq 5M_1^3M_2^3\delta$ with probability that is larger than $1 - (M_1M_2)^{-2}$.

In our implementation, the location of transmit and receive antennas are randomly selected inside a limited aperture that is bounded by the automotive radar form factor. The locations of antenna elements in the resulting virtual array are random as well, thereby acting as a random sub-Nyquist sampler of the corresponding ULA or URA. In the underlying problem, therefore, when the input SNR is high and the number of random sparse array elements satisfies the condition specified in (27) or (28), the recovered Hankel or block Hankel matrix is close to the true Hankel or block Hankel matrix corresponding to ULA or URA array response, respectively.

B. Discussion on Sparse Array Topology and Identifiability

In this section we examine the sampling strategies, i.e., SLA topologies that can guarantee unique completion of the low-rank Hankel matrix $\mathbf{Y}$.

Let us look at an example of two SLA configurations shown in Fig. 5(a). Both SLAs have the same number of array elements and the same aperture size of 3λ. The second SLA is a ULA with interelement spacing $d = \lambda$. Assume that a single target located at angle θ and let $\gamma \triangleq e^{j2\pi\frac{d}{\lambda}\sin\theta}$. The normalized array snapshot of a ULA with aperture size of 3λ is $\mathbf{y} = [1, \gamma, \gamma^2, \gamma^3, \gamma^4, \gamma^5, \gamma^6]^T$. The array snapshots of the two SLAs are $\mathbf{y}_1 = [1, \gamma, *, \gamma^3, *, *, \gamma^6]^T$ and $\mathbf{y}_2 = [1, *, \gamma^2, *, \gamma^4, *, \gamma^6]^T$, respectively, where $*$ denotes the missing elements. For the above two different SLAs, the Hankel matrices with missing elements are

$$\mathbf{Y}_1 = \begin{bmatrix} 1 & \gamma & * & \gamma^3 \\ \gamma & * & \gamma^3 & * \\ * & \gamma^3 & * & * \\ \gamma^3 & * & * & \gamma^6 \end{bmatrix}, \quad \mathbf{Y}_2 = \begin{bmatrix} 1 & * & \gamma^2 & * \\ * & \gamma^2 & * & \gamma^4 \\ \gamma^2 & * & \gamma^4 & * \\ * & \gamma^4 & * & \gamma^6 \end{bmatrix}.$$

Matrix $\mathbf{Y}$ is rank one and can be reconstructed from $\mathbf{Y}_1$ uniquely. However, there would be infinite completions of $\mathbf{Y}$ from $\mathbf{Y}_2$. In a ULA with element spacing $d = \lambda$, there is angle ambiguity which cannot be mitigated via matrix completion.

Let $\mathcal{G} = (V, E)$ be a bipartite graph associated with the sampling operator $\mathcal{P}_\Omega$, where $V = \{1, 2, \cdots, N\} \cup \{1, 2, \cdots, N\}$ and $(i, j) \in E$ iff $(i, j) \in \Omega$. Let $\mathbf{G} \in \mathbb{R}^{N\times N}$ be the biadjacency matrix of the bipartite graph $\mathcal{G}$ with $\mathbf{G}_{ij} = 1$ iff $(i, j) \in \Omega$. Note that $\mathcal{P}_\Omega(\mathbf{Y}) = \mathbf{Y} \odot \mathbf{G}$, where $\odot$ denotes the Hadamard product. The two bipartite graphs, $\mathcal{G}_1$ and $\mathcal{G}_2$ associated with the two SLAs are shown in Figs. 5(b) and 5(c), respectively. It can be seen that $\mathcal{G}_1$ is connected, while $\mathcal{G}_2$ is not. For a unique reconstruction of $\mathbf{Y}$, the graph must be connected [68].

Note the connectivity of the bipartite graph associated with the sampling operator $\mathcal{P}_\Omega$ is a necessary condition for matrix completion. Sufficient conditions of matrix completion involve the matrix coherence properties and the spectral gap of the graph $\mathcal{G}$, which is defined as the difference $\sigma_1(\mathbf{G}) - \sigma_2(\mathbf{G})$ between the largest singular value $\sigma_1(\mathbf{G})$ and the second largest singular value $\sigma_2(\mathbf{G})$ of $\mathbf{G}$ [69]. If the spectral gap of

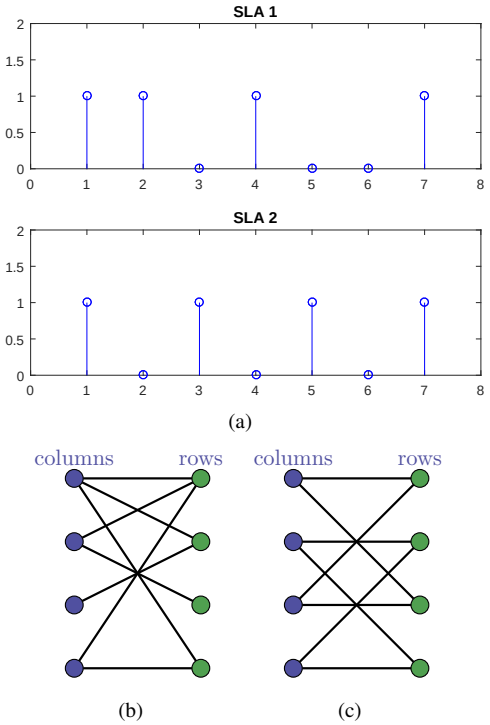

Figure 5: Examples of SLAs: (a) two SLAs and the corresponding bipartite graphs (b) $\mathcal{G}_1$ and (c) $\mathcal{G}_2$.

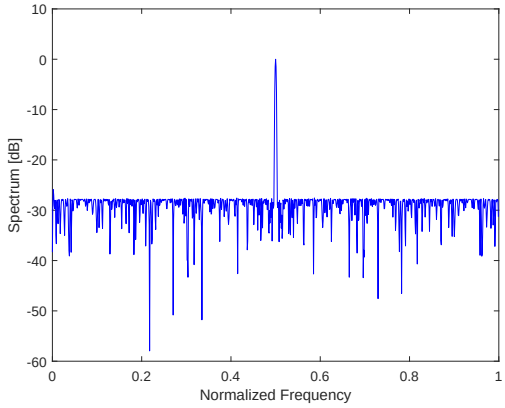

Figure 6: The spectrum of the optimized weights.

matrix $\mathbf{G}$ is sufficiently large, the nuclear norm minimization method defined in (14) exactly recovers the low-rank matrix satisfying conditions **B**1) and **B**2). It can be verified that $\mathcal{G}_2$ depicted in Fig. 5(c) is a 2-regular graph with vertex connectivity $\sigma_1(\mathbf{G}) = \sigma_2(\mathbf{G}) = 2$. Thus the spectral gap of $\mathbf{G}_2$ is zero and $\mathbf{Y}$ cannot be recovered from $\mathbf{Y}_2$.

Let $\mathcal{G}^{-1}_{K+1,K+1}$ denote the complete bipartite graph with $(K+1)\times(K+1)$ vertices minus one edge. Graph $\mathcal{G}$ is called a K-closed bipartite graph if $\mathcal{G}$ does not contain a vertex set whose induced subgraph is isomorphic to $\mathcal{G}^{-1}_{K+1,K+1}$. In general, a rank-$K$ matrix can be uniquely completed only if the bipartite graph $\mathcal{G}$ associated with the sampling is K-closable [68]. It was shown in [69] that if Ω is generated from a d-regular graph $\mathcal{G}$ with a sufficiently large spectra gap and $d \geq 36C^2\mu_0^2K^2$, then the nuclear norm optimization of (14) exactly recovers the low-rank matrix, where C is a constant. It can be seen that, if the coherence of $\mathbf{Y}$, i.e., μ_0 defined in Theorem 1, is low, the required number of observation samples or array elements of the SLA is small.

The spectra gap condition provides a guidance for choosing the location of sparse array elements. The sparse arrays can be optimized such that the bipartite graph associated with the sampling operator $\mathcal{P}_\Omega$, i.e., the locations of virtual array elements, has a large spectra gap. Detailed discussions are beyond the scope of this paper and will be left for our future work.

V. Numerical Results

In this section, we conduct numerical simulations to evaluate the performance of the proposed joint sparse spectrum and sparse arrays approach for high fidelity 4D sensing for automotive applications.

A. Range-Doppler Spectrum Under RSSFW

To demonstrate the performance of range and Doppler estimation using the proposed RSSFW, for one burst cycle, $N = 300$ pulses are transmitted on carriers that are uniformly at randomly chosen over $[f_c, f_c + B]$. The start carrier frequency is $f_c = 77$ GHz, and the effective bandwidth is set to $B = 200$ MHz, corresponding to range resolution of $\Delta R = 0.75$ m. The pulse duration is $T_p = 25$ ns and the step

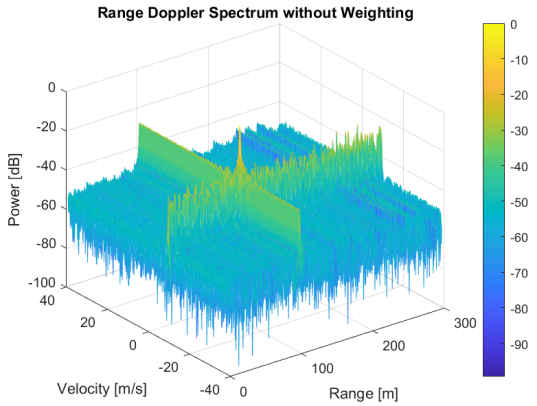

(a)

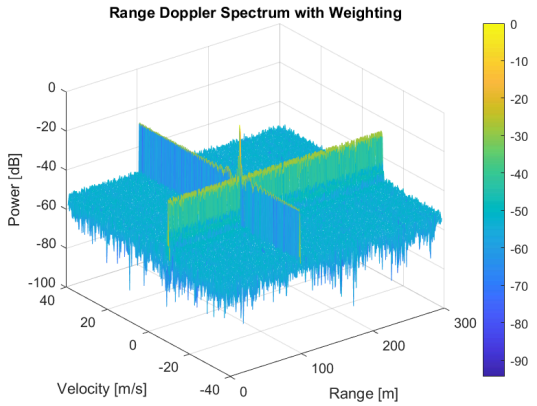

(b)

Figure 7: Illustration of range and Doppler spectrum for two targets with equal power located at range of 100 m with velocity of -10 m/s. (a) spectra without weighting; (b) spectra with weighting.

frequency is $\Delta f = 0.5$ MHz. The maximum unambiguous detectable range is $R_u = 300$ m. The burst cycle repetition interval is $T = 25$ μs. The maximum unambiguous detectable velocity is $v_{\max} = \lambda/(4T) = 38.96$ m/s. To measure the target velocity, $M = 300$ burst cycles are carried out with a dwell time of $MT = 7.5$ ms, rendering a velocity resolution of $\Delta v = \lambda/(2MT) = 0.26$ m/s. To achieve waveform orthogonality among transmit antennas, a Chu sequence [70] of length $M = 307$ was generated and then truncated into length $M = 300$ for phase coding in slow time. The SNR of the demodulated echo signals at receiver is set to 10 dB. To suppress the high range sidelobes, the weights obtained by solving the optimization problem (10) are multiplied to the fast-time samples corresponding to sparse carrier frequencies.

We first consider two targets with equal RCS at the same range of $R = 100$ m and with the same velocity of $v = -10$ m/s but different angles. To demonstrate waveform orthogonality of RSSFW through DDM, we consider a simple two transmit antenna scenario. At each receive antenna, the received echo signal is the superposition of the signals transmitted from multiple transmit antennas reflected by the two targets.

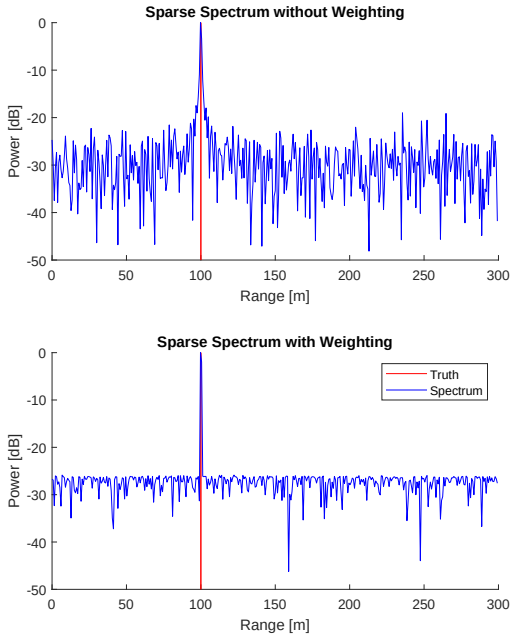

Figure 8: Comparison of the range spectrum of random sparse step-frequency automotive radar with and without weighting for two targets with equal power located at the same range of $R = 100$ m.

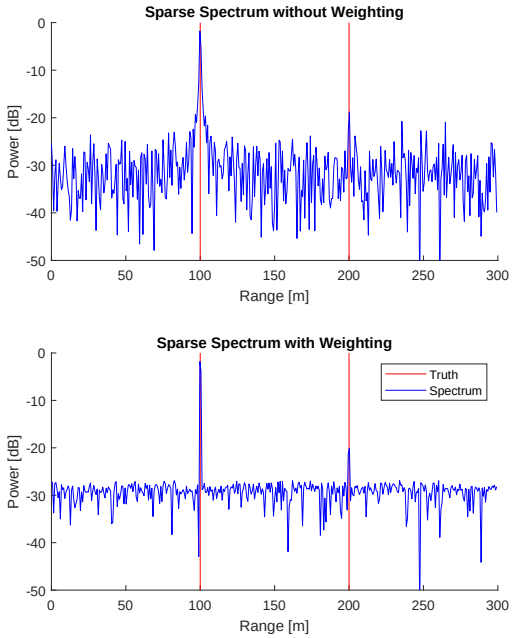

Figure 9: Comparison of range spectrum with and without weighting. Two targets are located at different ranges of 100 m and 200 m with normalized power of 1 and 0.1, respectively.

The target range-Doppler spectrum is obtained by carrying out IDFT on the burst pulse samples, followed by demodulation and DFT operation along the slow time.

Fig. 6 shows the spectrum obtained from the optimized weights for the radar parameters defined above. It can be seen that the spectrum is upper bounded by -27.5 dB over the entire sidelobe region.

Figs. 7(a) and 7(b) show the range-Doppler spectrum of the two targets with and without weighting, respectively. It is seen that there is a flat Doppler ridge over the whole Doppler domain corresponding to the target range bin of $R = 100$ m. This Doppler ridge is the waveform residual from the other transmit antennas after demodulation in slow time. The range spectrum corresponding to the Doppler bin of -10 m/s is shown in Fig. 8. It can be seen in both Figs. 7 and 8 that, without weighting, there are high sidelobes at certain locations in the range spectrum due to the sparse spectrum utilization in RSSFW, whereas the PSL over the entire unambiguous detectable range is minimized after weighting.

Next, we consider two targets at different ranges of $R_1 = 100$ m and $R_2 = 200$ m but with the same velocity of -10m/s. The two targets have different RCS such that in the echo samples, the signal power of the target at range R_2 is only 10% of that of the target at range R_1. The range spectrum of these two targets is shown in Fig. 9. It can be seen that the high range sidelobes may easily mask the target with small RCS. In other words, without introducing high probability of false alarm, the weak target cannot be detected. On the contrary, the weak target is reliably detected after the range PSL is minimized with weighting.

B. One-Dimensional Sparse Array Completion

To achieve high azimuth angular resolution, multiple automotive radar transceivers are cascaded together to synthesize a large sparse array in azimuth. Here, we consider the same physical array shown in Fig. 2, where $M_t = 6$ transmit and $M_r = 8$ receive antennas are placed in an interleaved way along the horizontal direction at

$$l_{\mathrm{TX}} = [1, 19, 37, 55, 79, 91]\,\lambda/2,$$
$$l_{\mathrm{RX}} = [12, 22, 25, 39, 58, 62, 70, 73]\,\lambda/2.$$

A virtual array with total 48 elements is synthesized. The transmit and receive antennas as well as the virtual array are plotted in Fig. 2.

Two targets are at the same range $R = 100$ m with velocity of $v = -10$ m/s. Their respective azimuth angles are $\theta_1 = 0^\circ$ and $\theta_2 = 20^\circ$. The two targets are first separated in range-Doppler with the RSSFW. The complex peak values in the range-Doppler spectrum corresponding to every virtual sparse array consists of an array snapshot for azimuth angle finding.

The virtual SLA shown in Fig. 2 acts as a deterministic sampler of a rank-2 Hankel matrix $\mathbf{Y} \in \mathbb{C}^{N\times N}$ with $N = 76$, which is constructed based on the array response of a ULA with 152 elements. The array response of the SLA is normalized by its first element. Based on the observed SLA response, the Hankel matrix $\mathbf{Y}$ is completed via the singular value thresholding (SVT) algorithm [55]. Let $\hat{\mathbf{Y}}$ denote the completed Hankel matrix. The full ULA response can be reconstructed by taking the average of the anti-diagonal elements of matrix $\hat{\mathbf{Y}}$. The completed full array has an aperture size of 76λ. Intuitively, in this simulation setting, matrix

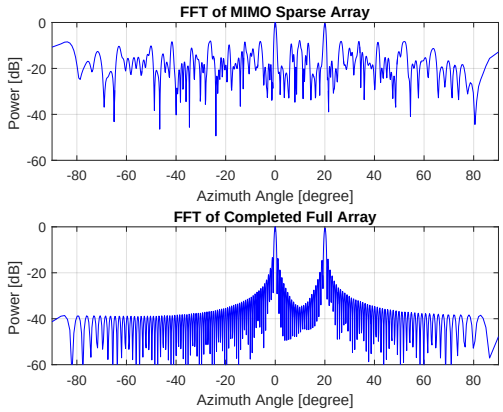

Figure 10: The spectrum of two targets with azimuth angles of $\theta_1 = 0^\circ$ and $\theta_2 = 20^\circ$ degree under MIMO sparse array and fully completed array.

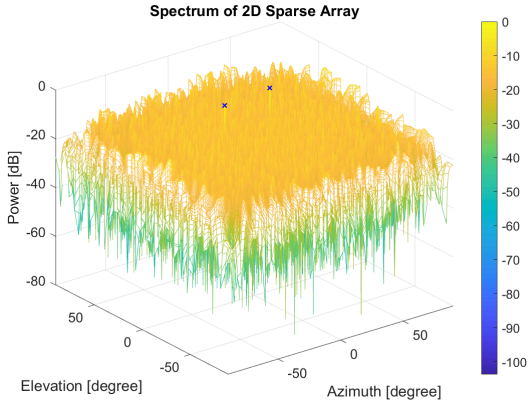

Figure 11: The spectrum of two targets with azimuth and elevation angles of $(\chi_1, \varphi_1) = (-20^\circ, 5^\circ), (\chi_2, \varphi_2) = (20^\circ, 10^\circ)$ under the sparse array. The targets' angles are marked with crosses. There are high sidelobes in the spectrum due to the existing of large number of holes in the sparse array.

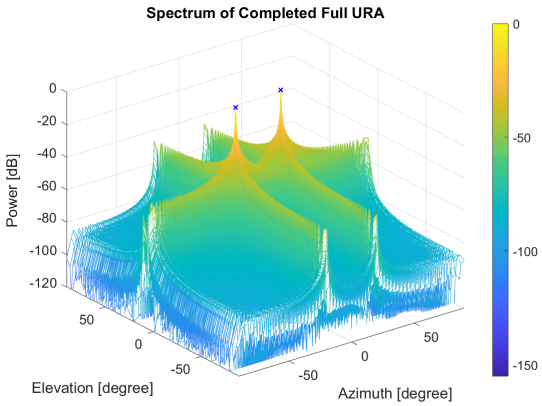

Figure 12: The spectrum of two targets with azimuth and elevation angles of $(\chi_1, \varphi_1) = (-20^\circ, 5^\circ), (\chi_2, \varphi_2) = (20^\circ, 10^\circ)$ under the completed full URA. The targets' angles are marked with crosses.

completion contributes around $10 \log 10 \, (152/48) \approx 5$ dB SNR improvement for array processing.

In Fig. 10, we plot the angle spectrum for the two targets. The two azimuth angle spectra are obtained by applying FFT to the original SLA with the holes filled with zeros and to the full array completed via matrix completion, respectively. It is found that the FFT of the SLA generates two peaks corresponding to the correct azimuth directions at a cost of high sidelobes, and thus it is difficult to detect the two targets in azimuth directions under the original SLA. On the contrary, the completed full array shows two clear peaks corresponding to correct azimuth locations in the angle spectrum, and the sidelobes are greatly suppressed in the completed full array.

C. Two-Dimensional Sparse Array Completion

We consider the same 2D physical array shown in Fig. 3 for joint high-resolution azimuth and elevation angle estimation, by cascading 4 automotive radar transceivers. These 12 transmit antennas and 16 receive antennas are randomly deployed in an area of $[0, 100(\lambda/2)] \times [0, 120(\lambda/2)]$ to synthesize a 2D MIMO virtual array of 196 elements. The cascaded automotive radar form factor is around 20×24 cm. In Fig. 3, the dimension of the 2D sparse array is $D_y \times D_x = 183(\lambda/2) \times 194(\lambda/2)$. A total number of $35,502$ elements are required to construct a URA of the same dimension with half-wavelength interelement spacing. In other words, the virtual sparse array only occupies 0.54% the total elements of the URA.

Two targets with the same range and Doppler bin are considered. Their angles to the x and y directions are $(\chi_1, \varphi_1) = (-20^\circ, 5^\circ), (\chi_2, \varphi_2) = (20^\circ, 10^\circ)$, respectively. The sparse array snapshot is consisted of the complex peak values in the range-Doppler spectrum corresponding to each sparse array element. The input SNR of the array response is set to 20 dB, which is reasonable in automotive radar because the fast-time and slow-time coherent processing provides a high processing gain, as stated in Section II-A. We then construct a block Hankel matrix $\mathbf{Y}_E$ of dimension $9,009 \times 8,928$ using one array snapshot of this 2D sparse array with 196 elements. Only 0.78% of the Hankel matrix entires are non-zero. Based on one snapshot of 2D sparse array, the block Hankel matrix is completed via the SVT algorithm and the full URA is then obtained. In this simulation setting, matrix completion contributes around $10 \log 10 \, (35,502/196) \approx 22.5$ dB SNR gain for array processing.

Figs. 11 and 12 plot the azimuth-elevation spectra of the two targets under the 2D sparse array and the completed full URA, respectively. It is found that both sparse array and URA generate two peaks corresponding to the correct azimuth and elevation angles of the targets. However, in the azimuth-elevation spectrum of 2D sparse array, there are high sidelobes over the entire azimuth and elevation FOVs. On the contrary, the high sidelobes are mitigated in the completed URA.

VI. Conclusions

In this paper, we developed a new automotive radar system utilizing a thinned frequency spectrum to synthesize a large effective bandwidth for high range resolution profiles. The

RSSFW MIMO radar is considered for 2D sparse arrays with hundreds of virtual elements. Sensor interpolation was exploited to recover missing elements in the sparse arrays using matrix completion. Numerical simulation verified that the proposed imaging radar yields high performance for joint high-resolution azimuth and elevation angle estimation.

APPENDIX A
PROOF OF THEOREM 1

Proof. The Hankel matrix $\mathbf{Y}$ has a Vandermonde decomposition structure, i.e., $\mathbf{Y} = \mathbf{B}\mathbf{\Sigma}\mathbf{B}^T$. The compact singular value decomposition of $\mathbf{Y}$ is expressed as $\mathbf{Y} = \mathbf{U}\mathbf{\Lambda}\mathbf{V}^H$, where $\mathbf{U} \in \mathbb{C}^{N\times K}$ and $\mathbf{V} \in \mathbb{C}^{N\times K}$ such that $\mathbf{U}^H\mathbf{U} = \mathbf{I}_K$ and $\mathbf{V}^H\mathbf{V} = \mathbf{I}_K$, and $\mathbf{\Lambda} \in \mathbb{R}^{K\times K}$ is a diagonal matrix containing the singular values of $\mathbf{Y}$. Following the same QR decomposition of manifold matrix $\mathbf{B}$ utilized in [65], [71], we can show that $\mu(U)$ and $\mu(V)$ defined in (25) are related only to the array manifold matrix $\mathbf{B}$. The ULA configuration has element spacing of $d = \lambda/2$. Assume that the target angles in set $\{\theta_k\}_{k\in\mathbb{N}_K^+}$ are distinct with a minimal spatial frequency separation $x = \min\limits_{(i,j)\in\mathbb{N}_K^+\times\mathbb{N}_K^+, i\neq j} \frac{d}{\lambda}\left(\sin\theta_i - \sin\theta_j\right)$ satisfying $|x| \geq \xi \neq 0$. If $K \leq \frac{N}{\sqrt{\beta_N(\xi)}}$ holds, where $\beta_N(\xi) = \frac{1}{N}\frac{\sin^2(\pi N\xi)}{\sin^2(\pi\xi)}$ is the Fejér kernel, it was shown in [65], [71] that

$$\mu(U) = \mu(V) \leq \frac{\sqrt{N}}{\sqrt{N} - (K-1)\sqrt{\beta_N(\xi)}}. \tag{29}$$

Consequently, $\mu_0 \triangleq \frac{\sqrt{N}}{\sqrt{N}-(K-1)\sqrt{\beta_N(\xi)}}$ and $\mu_1 \triangleq \mu_0\sqrt{K}$ hold true with probability 1. □

REFERENCES

[1] S. Sun and A. P. Petropulu, "A sparse linear array approach in automotive radars using matrix completion," in *Proc. IEEE Int. Conf. Acoust., Speech, Signal Process. (ICASSP)*, Barcelona, Spain, May 2020.

[2] S. Sun and Y. D. Zhang, "Four-dimensional high-resolution automotive radar imaging exploiting joint sparse-frequency and sparse-array design," in *Proc. IEEE Int. Conf. Acoust., Speech, Signal Process. (ICASSP)*, Toronto, Canada, June 2021.

[3] U.S. Department of Transportation's National Highway Traffic Safety Administration (NHTSA), "2016 fatal motor vehicle crashes: Overview," [Available Online] https://www.nhtsa.gov/press-releases/usdot-releases-2016-fatal-traffic-crash-data, Oct. 6, 2017.

[4] L. Ecola, S. W. Popper, R. Silberglitt, and L. Fraade-Blanar, "The road to prepared for a vision for achieving zero roadway deaths by 2050," RAND Corporation Report, [Available Online] https://www.rand.org/pubs/research_reports/RR2333.html, April 18, 2018.

[5] R. Gourova, O. Krasnov, and A. Yarovoy, "Analysis of rain clutter detections in commercial 77 GHz automotive radar," in *Proc. 14th European Radar Conference (EuRAD)*, Nuremberg, Germany, Oct. 2017.

[6] S. Patole, M. Torlak, D. Wang, and M. Ali, "Automotive radars: A review of signal processing techniques," *IEEE Signal Process. Mag.*, vol. 34, no. 2, pp. 22–35, 2017.

[7] F. Engels, P. Heidenreich, A. M. Zoubir, F. Jondral, and M. Wintermantel, "Advances in automotive radar: A framework on computationally efficient high-resolution frequency estimation," *IEEE Signal Process. Mag.*, vol. 34, no. 2, pp. 36–46, 2017.

[8] S. Sun, A. P. Petropulu, and H. V. Poor, "MIMO radar for advanced driver-assistance systems and autonomous driving: Advantages and challenges," *IEEE Signal Process. Mag.*, vol. 37, no. 4, pp. 98–117, 2020.

[9] A. Kamann and *et. al.*, "Automotive radar multipath propagation in uncertain environments," in *Proc. Intl. Conf. Intelligent Transportation Systems (ITSC)*, Maui, Hawaii, Nov. 2018.

[10] I. Bilik and *et al.*, "Automotive MIMO radar for urban environments," in *Proc. IEEE Radar Conf.*, Philadelphia, PA, May 2016.

[11] F. Meinl, M. Stolz, M. Kunert, and H. Blume, "An experimental high performance radar system for highly automated driving," in *Proc. Intl. Conf. Microwaves for Intelligent Mobility (ICMIM)*, Nagoya, Japan, Mar. 2017.

[12] S. Alland and *et al.*, "Virtual radar configuration for 2D array," U.S. Patent 9 869 762, Jan. 16, 2018.

[13] C. R. Qi, H. Su, K. Mo, and L. J. Guibas, "PointNet: Deep learning on point sets for 3D classification and segmentation," in *Proc. IEEE Conf. Computer Vision and Pattern Recognition (CVPR)*, Honolulu, HI, July 2017.

[14] C. R. Qi, L. Yi, H. Su, and L. J. Guibas, "PointNet++: Deep hierarchical feature learning on point sets in a metric space," in *Proc. Conf. Neural Information Processing Systems (NIPS)*, Long Beach, CA, Dec. 2017.

[15] M. A. Richards, *Fundamentals of Radar Signal Processing, 2nd Ed.* New York, NY: McGraw-Hill, 2014.

[16] L. Zheng, Q. Liu, X. Wang, and A. Maleki, "ℓ_p-based complex approximate message passing with application to sparse stepped frequency radar," *Signal Processing*, vol. 134, pp. 249–260, 2017.

[17] K. V. Mishra, S. Mulleti, and Y. C. Eldar, "RaSSteR: Random sparse step-frequency radar," [Available Online] https://arxiv.org/pdf/2004.05720.pdf, April, 2020.

[18] E. J. Candès and T. Tao, "The Dantzig selector: Statistical estimation when p is much larger than n," *The Annals of Statistics*, vol. 35, no. 6, pp. 2313–2351, 2007.

[19] J. Li and P. Stoica, "MIMO radar with colocated antennas," *IEEE Signal Process. Mag.*, vol. 24, no. 5, pp. 106–114, 2007.

[20] I. Bilik and *et al.*, "Automotive multi-mode cascaded radar data processing embedded system," in *Proc. IEEE Radar Conf.*, Oklahoma City, OK, April 2018.

[21] V. Giannini and *et al.*, "A 192-virtual-receiver 77/79 GHz GMSK code-domain MIMO radar system-on-chip," in *Proc. IEEE Intl. Solid-State Circuits Conf. (ISSCC)*, San Francisco, CA, Feb. 17-21, 2019.

[22] Texas Instruments Inc., "Design guide: TIDEP-01012 imaging radar using cascaded mmWave sensor reference design," [Available Online] https://www.ti.com/lit/ug/tiduen5a/tiduen5a.pdf, Mar. 2020.

[23] https://www.zf.com/products/en/cars/products_58368.html, May 2021.

[24] https://www.continental-automotive.com, May 2021.

[25] C. Schmid, R. Feger, C. Wagner, and A. Stelzer, "Design of a linear non-uniform antenna array for a 77-GHz MIMO FMCW radar," in *Proc. IEEE MTT-S Intl. Microwave Workshop on Wireless Sensing, Local Positioning, and RFID*, Cavtat, Croatia, Sept. 2009.

[26] J. Searcy and S. Alland, "MIMO antenna with elevation detection," U.S. Patent 9 541 639 B2, Jan. 10, 2017.

[27] R. Rajamaki, S. P. Chepuri, and V. Koivunen, "Hybrid beamforming for active sensing using sparse arrays," *IEEE Trans. Signal Process.*, vol. 68, pp. 6402–6417, 2020.

[28] C.-Y. Chen and P. P. Vaidyanathan, "Minimum redundancy MIMO radars," in *Proc. IEEE Intl. Symposium on Circuits and Systems (ISCAS)*, Seattle, WA, May 18-21, 2008.

[29] P. Pal and P. P. Vaidyanathan, "Nested arrays: A novel approach to array processing with enhanced degrees of freedom," *IEEE Trans. Signal Process.*, vol. 58, no. 8, pp. 4167–4181, 2010.

[30] P. P. Vaidyanathan and P. Pal, "Sparse sensing with co-prime samplers and arrays," *IEEE Trans. Signal Process.*, vol. 59, no. 2, pp. 573–586, 2011.

[31] S. Qin, Y. D. Zhang, and M. G. Amin, "Generalized coprime array configurations for direction-of-arrival estimation," *IEEE Trans. Signal Process.*, vol. 63, no. 6, pp. 1377–1390, 2015.

[32] M. Wang and A. Nehorai, "Coarrays, MUSIC, and the Cramer-Rao bound," *IEEE Trans. Signal Process.*, vol. 65, no. 4, pp. 933–946, 2017.

[33] C.-L. Liu and P. P. Vaidyanathan, "Super nested arrays: Linear sparse arrays with reduced mutual coupling - Part I: Fundamentals," *IEEE Trans. Signal Process.*, vol. 64, no. 15, pp. 3997–4012, 2016.

[34] ——, "Super nested arrays: Linear sparse arrays with reduced mutual coupling - Part II: High-order extensions," *IEEE Trans. Signal Process.*, vol. 64, no. 16, pp. 4203–4217, 2016.

[35] H. Qiao and P. Pal, "Guaranteed localization of more sources than sensors with finite snapshots in multiple measurement vector models using difference co-arrays," *IEEE Trans. Signal Process.*, vol. 67, no. 22, pp. 5715–5729, 2019.

[36] P. Hacker and B. Yang, "Single snapshot DOA estimation," *Advances in Radio Science*, vol. 8, pp. 251–256, 2010.

[37] J. Shi, F. Wen, and T. Liu, "Nested MIMO radar: Coarrays, tensor modeling and angle estimation," *IEEE Trans. Aerosp. Electron. Syst.*, in press.
[38] P. Pal and P. P. Vaidyanathan, "Coprime sampling and the MUSIC algorithm," in *Proc. Digital Signal Processing and Signal Processing Education Meeting (DSP/SPE)*, Sedona, AZ, Jan. 4-7, 2011.
[39] C.-L. Liu and P. P. Vaidyanathan, "Remarks on the spatial smoothing step in coarray MUSIC," *IEEE Signal Process. Lett.*, vol. 22, no. 9, pp. 1438–1442, 2015.
[40] H. Qiao and P. Pal, "Unified analysis of co-array interpolation for direction-of-arrival estimation," in *Proc. IEEE Int. Conf. Acoust., Speech, Signal Process. (ICASSP)*, New Orleans, LA, May 2017.
[41] D. Romero, D. D. Ariananda, Z. Tian, and G. Leus, "Compressive covariance sensing: Structure-based compressive sensing beyond sparsity," *IEEE Signal Process. Mag.*, vol. 33, no. 1, pp. 78–93, 2016.
[42] S. Qin, Y. D. Zhang, M. G. Amin, and A. M. Zoubir, "Generalized coprime sampling of Toeplitz matrices for spectrum estimation," *IEEE Signal Process. Mag.*, vol. 65, no. 1, pp. 81–94, 2017.
[43] H. Qiao and P. Pal, "Gridless line spectrum estimation and low-rank Toeplitz matrix compression using structured samplers: A regularization-free approach," *IEEE Trans. Signal Process.*, vol. 65, no. 9, pp. 2221–2236, 2017.
[44] C. Zhou, Y. Gu, X. Fan, Z. Shi, G. Mao, and Y. D. Zhang, "Direction-of-arrival estimation for coprime array via virtual array interpolation," *IEEE Trans. Signal Process.*, vol. 66, no. 22, pp. 5956–5971, 2018.
[45] T. Spreng and *et al.*, "Wideband 120 GHz to 140 GHz MIMO radar: System design and imaging results," in *Proc. European Microwave Conf. (EuMC)*, Paris, France, Sept. 2015.
[46] C. Zhou, Y. Gu, Z. Shi, and Y. D. Zhang, "Off-grid direction-of-arrival estimation using coprime array interpolation," *IEEE Signal Process. Lett.*, vol. 25, no. 11, pp. 1710–1714, 2018.
[47] S. Zhang, A. Ahmed, Y. D. Zhang, and S. Sun, "DOA estimation exploiting interpolated multi-frequency sparse array," in *Proc. IEEE Workshop on Sensor Array and Multichannel Processing (SAM)*, Hangzhou, China, June 2020.
[48] Y. Chi, L. L. Scharf, A. Pezeshki, and A. R. Calderbank, "Sensitivity to basis mismatch in compressed sensing," *IEEE Trans. Signal Process.*, vol. 59, no. 5, pp. 2182–2195, 2011.
[49] M. Grant and S. Boyd, "CVX: Matlab software for disciplined convex programming, version 2.1," http://cvxr.com/cvx, Mar. 2014.
[50] V. F. Mecca, D. Ramakrishnan, and J. L. Krolik, "MIMO radar space-time adaptive processing for multipath clutter mitigation," in *Proc. IEEE Workshop on Sensor Array and Multichannel Processing (SAM)*, Waltham, MA, July 2006.
[51] J. Ying, J. F. Cai, D. Guo, G. Tang, Z. Chen, and X. Qu, "Vandermonde factorization of Hankel matrix for complex exponential signal recovery-application in fast NMR spectroscopy," *IEEE Trans. Signal Process.*, vol. 66, no. 21, pp. 5520–5533, 2018.
[52] E. J. Candès and B. Recht, "Exact matrix completion via convex optimization," *Foundations of Computational Mathematics*, vol. 9, no. 6, pp. 717–772, 2009.
[53] Velodyne, "HDL-32E high definition real-time LiDAR," datasheet, [Available Online] https://velodynelidar.com/products/hdl-32e/, 2021.
[54] Y. Hua, "Estimating two-dimensional frequencies by matrix enhancement and matrix pencil," *IEEE Trans. Signal Process.*, vol. 40, no. 9, pp. 2267–2280, 1992.
[55] J. F. Cai, E. J. Candès, and Z. Shen, "A singular value thresholding algorithm for matrix completion," *SIAM J. Optim.*, vol. 20, no. 2, pp. 1956–1982, 2010.
[56] Y. Hua and T. K. Sarkar, "Matrix pencil method for estimating parameters of exponentially damped/undamped sinusoids in noise," *IEEE Trans. Acoust., Speech, Signal Process.*, vol. 38, no. 5, pp. 814–824, 1990.
[57] P. Barton, "Digital beam forming for radar," *IEE Proc. F - Commun., Radar and Signal Processing*, vol. 127, no. 4, 1980.
[58] R. Schmidt, "Multiple emitter location and signal parameter estimation," *IEEE Trans. Antennas Propag.*, vol. 34, no. 3, pp. 276–280, 1986.
[59] R. Roy and T. Kailath, "ESPRIT – estimation of signal parameters via rotation invariance techniques," *IEEE Trans. Acoust., Speech, Signal Process.*, vol. 17, no. 7, pp. 984–995, 1989.
[60] T. Strohmer and B. Friedlander, "Compressed sensing for MIMO radar - algorithms and performance," in *Proc. Asilomar Conf. Signals, Syst. Comput.*, Pacific Grove, CA, Nov. 2009.
[61] Y. Yu, A. P. Petropulu, and H. V. Poor, "MIMO radar using compressive sampling," *IEEE J. Sel. Topics Signal Process.*, vol. 4, no. 1, pp. 146–163, 2010.
[62] Y. D. Zhang, M. G. Amin, and B. Himed, "Sparsity-based DOA estimation using co-prime arrays," in *Proc. IEEE Int. Conf. Acoust., Speech, Signal Process. (ICASSP)*, Vancouver, Canada, May 2013.
[63] Y. Yu, S. Sun, R. N. Madan, and A. P. Petropulu, "Power allocation and waveform design for the compressive sensing based MIMO radar," *IEEE Trans. Aerosp. Electron. Syst.*, vol. 50, no. 2, pp. 898–909, 2014.
[64] S. Sun, W. U. Bajwa, and A. P. Petropulu, "MIMO-MC radar: A MIMO radar approach based on matrix completion," *IEEE Trans. Aerosp. Electron. Syst.*, vol. 51, no. 3, pp. 1839–1852, 2015.
[65] S. Sun and A. P. Petropulu, "Waveform design for MIMO radars with matrix completion," *IEEE J. Sel. Topics Signal Process.*, vol. 9, no. 8, pp. 1400–1411, 2015.
[66] E. J. Candès and Y. Plan, "Matrix completion with noise," *Proc. IEEE*, vol. 98, no. 6, pp. 925–936, 2010.
[67] Y. Chen and Y. Chi, "Robust spectral compressed sensing via structured matrix completion," *IEEE Trans. Inf. Theory*, vol. 60, no. 10, pp. 6576–6601, 2014.
[68] F. Király and R. Tomioka, "A combinatorial algebraic approach for the identifiability of low-rank matrix completion," in *Proc. Intl. Conf. Machine Learning (ICML)*, Edinburgh, Scotland, UK, June 2012.
[69] S. Bhojanapalli and P. Jain, "Universal matrix completion," in *Proc. Intl. Conf. Machine Learning (ICML)*, Beijing, China, June 2014.
[70] D. Chu, "Polyphase codes with good periodic correlation properties," *IEEE Trans. Inf. Theory*, vol. 18, no. 4, pp. 531–532, 1972.
[71] D. S. Kalogerias and A. P. Petropulu, "Matrix completion in colocated MIMO radar: Recoverability, bounds & theoretical guarantees," *IEEE Trans. Signal Process.*, vol. 62, no. 2, pp. 309–321, 2014.